Modeling Circumnuclear Dust Emission Using ALMA Observations of Early-type Galaxies

Edison Carlisle

A senior thesis submitted to the faculty of
Brigham Young University
in partial fulfillment of the requirements for the degree of

Bachelor of Science

Benjamin Boizelle, Advisor

Department of Physics and Astronomy

Brigham Young University

ABSTRACT

Modeling Circumnuclear Dust Emission Using ALMA Observations of Early-type Galaxies

Edison Carlisle
Department of Physics and Astronomy, BYU
Bachelor of Science

The archive for the Atacama Large Millimeter/submillimeter Array (ALMA) includes data for a large number of galaxies, including 100 early-type galaxies (ETGs). Many of these host circumnuclear, dusty disks with radii of a few $\times 100$ pc to a few kpc. Previous analysis of thermal dust emission in ETGs has been hampered by both poor sampling of the far-IR spectral energy distributions (SEDs) and coarse angular resolution, which blurs together thermal and non-thermal sources. With continuum imaging at high resolutions and sensitivities, the ALMA archive enables thermal emission measurements for frequencies in the Rayleigh-Jeans tails that are crucial in constraining their dust properties. Here, we demonstrate the power of ALMA by building SEDs using archival data of ETGs from telescopes across the UV to radio spectrum. Using `MPFIT`, a least-squares fitting function, as well as a Bayesian framework, we model the far-IR SEDs of these dusty disks with modified blackbody curves to determine the mass, temperature, and emissivity of the cold dust. We compare these results with parameters recovered from `CIGALE`, a full SED fitting function. We present SEDs and the accompanying corner plots of these galaxies, as well as the distribution of the masses, temperatures, and emissivity slopes. We also perform a non-isothermal analysis for NGC 6861, and find that an isothermal analysis is more efficient while producing similar results.

ACKNOWLEDGMENTS

Contents

List of Figures

List of Tables

Chapter 1

Introduction

1.1 Early-type Galaxies and their Interstellar Medium

In 1926, Edwin Hubble published the famous "Hubble Sequence," a method of classifying galaxies [1]. The Hubble Sequence divided galaxies into four major groups: elliptical galaxies, lenticular galaxies, spiral galaxies, and irregular galaxies (see Fig. 1.1). Elliptical galaxies appear smooth, round, and featureless, while spiral galaxies have disk-like features and distinct "arms" wound around the center. Lenticular galaxies lie somewhere in between. They have a distinct lens shape, but no obvious spiral structure. Irregular galaxies encompass all galaxies that do not fit into the previous categories. Elliptical and lenticular galaxies constitute early-type galaxies (ETGs), while spiral and irregular galaxies are classified as late-type galaxies. It is important to note that the "early" and "late" notations have no immediate relation to the age or evolution of the galaxy.

Each of the galaxies studied in this thesis are ETGs. Some ETGs are referred to as "red and dead." Major star-forming events for these ETGs ended billions of years ago. As a result, we only see old stars in these galaxies, which appear more red in color. Additionally, these galaxies usually have a depleted interstellar medium (ISM). The ISM is vital to star formation, as it consists of the
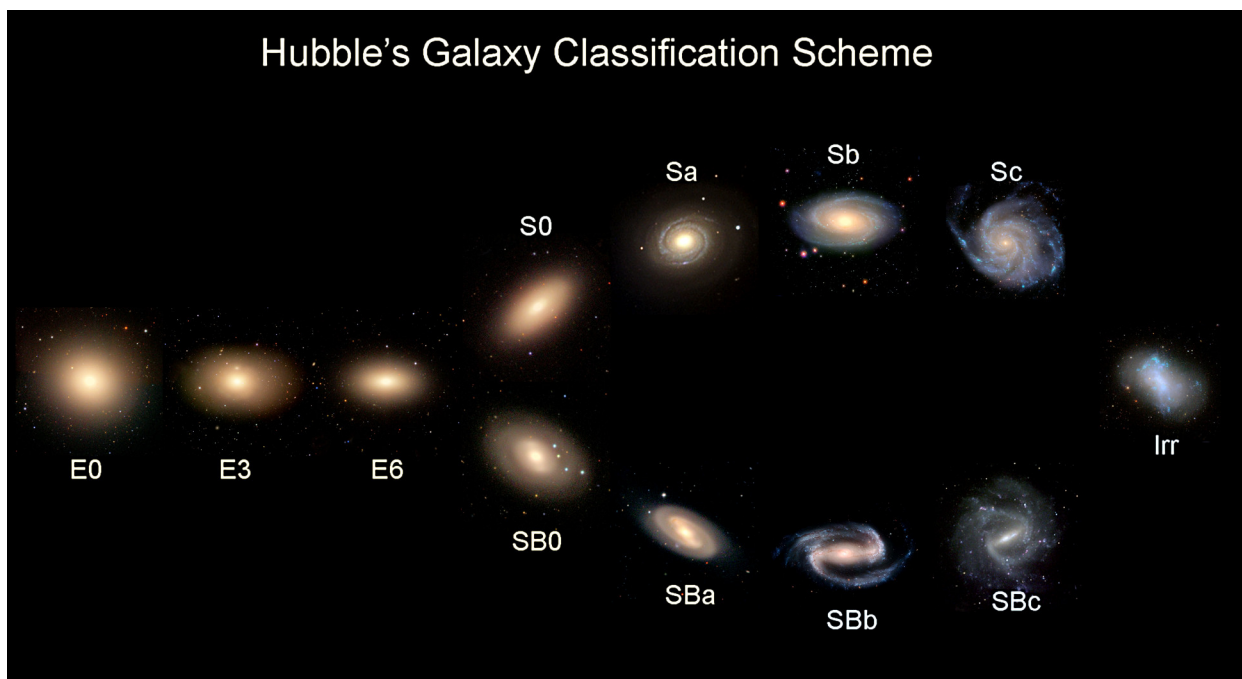
Figure 1.1 The Hubble Sequence classifies galaxies as elliptical (E0−7), lenticular (S0, SB0), spiral (Sa-Sc, SBa-SBc) or irregular (Irr). Credit: Galaxy Zoo [2].

gas and dust necessary to build stars. With a depleted ISM and therefore inadequate abundances of star-forming material, many early-type galaxies have no way of producing new stars, lending to the notion that these galaxies are "dead."

While the ISM of a typical ETG may not be rich enough to produce new stars, they are not devoid of all gas and dust. It is found that ~40% of ETGs outside galaxy clusters contain neutral atomic hydrogen, although the rate is much lower rate within clusters [3, 4]. Molecular gas, specifically carbon monoxide (CO), is detected in over 20% of ETGs [5]. Thermal dust emission has been detected in about a quarter of elliptical galaxies and half of lenticular galaxies. Typical dust masses range from 10^4 to 10^8 solar masses ($M_\odot$), with temperatures ranging from 15 to 35 K [6–8]. Warmer dust components have also been detected, with temperatures between 50 and 130 K [8], though the masses of these components are not significant in comparison to the cold dust component.

1.2   Circumnuclear Disks

Optical imaging with Hubble Space Telescope (HST) has found that about 10% of ETGs have dusty circumnuclear disks (CNDs) [9]. A significant portion of the gas and dust in these ETGs are found in their CNDs. These CNDs are morphologically regular, though some CNDs have filamentary structure. CNDs have semi-major axes ranging from 100 parsecs (pc, 1 pc = 3.086×10^{16} m) to a few kiloparsecs (kpc). This translates to an angular size of only a few arcseconds (1 arcsec = 1/3600 degrees). This small angular size makes CNDs difficult to resolve for most instruments, however HST and the Atacama Large Millimeter/submillimeter Array (ALMA) can achieve these resolutions (see Fig. 1.2).

The origin of CNDs could be either internal or external. CNDs that are misaligned or counter-rotating with respect to the rotation of the host galaxy are evidence of an externally sourced ISM, such as galactic merger events or tidal interactions. Filamentary dust features and warped

Figure 1.2 The CND of NGC 6861. The left image is optical imaging from HST [10], and the right image is CO(2-1) emission imaging from ALMA.

CNDs suggest that dust inflow from a recent merger process may have not yet settled. These features are found in a number of CNDs, suggesting that they could have formed due to external processes [9, 11]. However, dust grains are thought to be destroyed by heating and cosmic rays, giving them an estimated lifetime of $1-100 \times 10^6$ years [12, 13]. These time scales are too short to explain the existence of CNDs from merger events; any dust acquired from merger events should have been destroyed by now. It is possible that the dust could be shielded by cool clouds [13], however, this mechanism is not well understood.

There are a number of arguments for internal formation and retention of CNDs. It has been found from measurements of thermal dust emission and molecular gas emission lines that the gas reservoirs of lenticular galaxies are too large to be explained by minor merger events, as the galaxy would not be able to retain so much material [5, 8, 14]. CO emission line measurements show that a fraction of ETGs are found to have gas kinematics aligned with stellar kinematics

to within 10° [14–16]. This would be possible if the ISM formed alongside the stars rather than being sourced from outside the galaxy. Evolved stars can form dust grains in their atmospheres. Observations of ETGs suggest that mass loss from these evolved stars supplies the ISM with gas and dust [17]. However, dust mass does not correlate with stellar mass enough to suggest this applies to all ETGs [6, 8].

1.3 Modified Blackbody Function

To model the dust content in CNDs, it is common practice to use a modified blackbody (MBB) function, given by

$$S_\nu = \frac{\kappa_\nu M_d B(\nu, T_d)}{D^2}, \tag{1.1}$$

where $\kappa_\nu = \kappa_0 (\nu/\nu_0)^\beta$ and

$$B(\nu, T_d) = \frac{2h\nu^3}{c^2} \frac{1}{\exp(h\nu/kT_d) - 1}. \tag{1.2}$$

Here, the flux S_ν measured in Janskys (1 Jy = 10^{-26} W m^{-2} Hz^{-1}) emitted by dust is determined from the frequency ν that the dust is observed at, the dust mass and temperature M_d and T_d, the Planck function $B(\nu, T_d)$, the distance to the galaxy D, and the dust absorption coefficient κ_ν. The constants that appear in the Planck function are the speed of light c, the Planck constant h, and the Boltzmann constant k. As seen above, the absorption coefficient is frequency dependent. The frequency dependence follows a power-law with slope β, called the emissivity index. The consant κ_0 is used to normalize absorption at frequency ν_0. In this work, we use the values from Draine (2003) of $\kappa_0 = 1.92$ cm^2 g^{-1} at $\nu_0 = 856.6$ GHz (350 μm) [18]. We also use distance measurements from Tonry et al. (2001) [19] See Fig. 1.3 for a sample modified blackbody curve.

A property of blackbody emission is that the frequency of peak emission is temperature dependent. For this reason, blackbody emission can be referred to as thermal emission. Hotter objects peak at higher frequencies. Stars are bright enough that they peak at visible frequencies. Cooler

objects generally peak in the infrared (IR). CNDs are cold enough that they emit in the far-IR frequencies. By analyzing the emission at a range of frequencies, often called the spectral energy distribution (SED), we can begin to fit the MBB to data and recover M_d, T_d, and β. Previous surveys fix β to values 2.00 [6–8], however, laboratory measurements show that different carbonaceous and silicate forms of dust that match ISM observations have measured β values ranging from 1.2 to 2.3 [20, 21].

In the Rayleigh-Jeans regime of blackbody radiation, or the blackbody emission at frequencies significantly lower than the peak emission, the emission can be modeled with a power-law function. In the limit of lower-frequencies, the Rayleigh-Jeans law approximates the blackbody emission as

$$B(\nu, T_d) \approx \frac{2\nu^2 k T_d}{c^2}, \quad h\nu \ll kT_d. \tag{1.3}$$

Substituting this back into Equation 1.1 gives us

$$S_\nu \propto \nu^{\beta+2}. \tag{1.4}$$

This shows that β is vital to the power-law slope of the Rayleigh-Jeans regime ($\beta + 2$, also see Fig. 1.3). Thus, acquiring flux measurements for CNDs at low frequencies should help us constrain β rather than rely on fixed values. For a graphical representation of the Rayleigh-Jeans law, see Fig. 1.3.

Some problems arise concerning the degeneracies of different parameters. Both κ_0 and M_d are directly proportional to S_ν. If both parameters were fit simultaneously, we would find an inverse relationship between κ_0 and M_d where the value of one would completely depend on the value of the other. Thus, we assign κ_0 to the value above and acknowledge that recovered values of M_d depend on this assignment. A more subtle degeneracy is found between T_d and β. In the Rayleigh-Jeans regime, a negative correlation is found between T_d and β. This anti-correlation arises from common methods used to fit MBB functions [22]. Interestingly, there may also be physical correlations between β and T_d. Laboratory measurements show increasing β with decreasing T_d, again giving
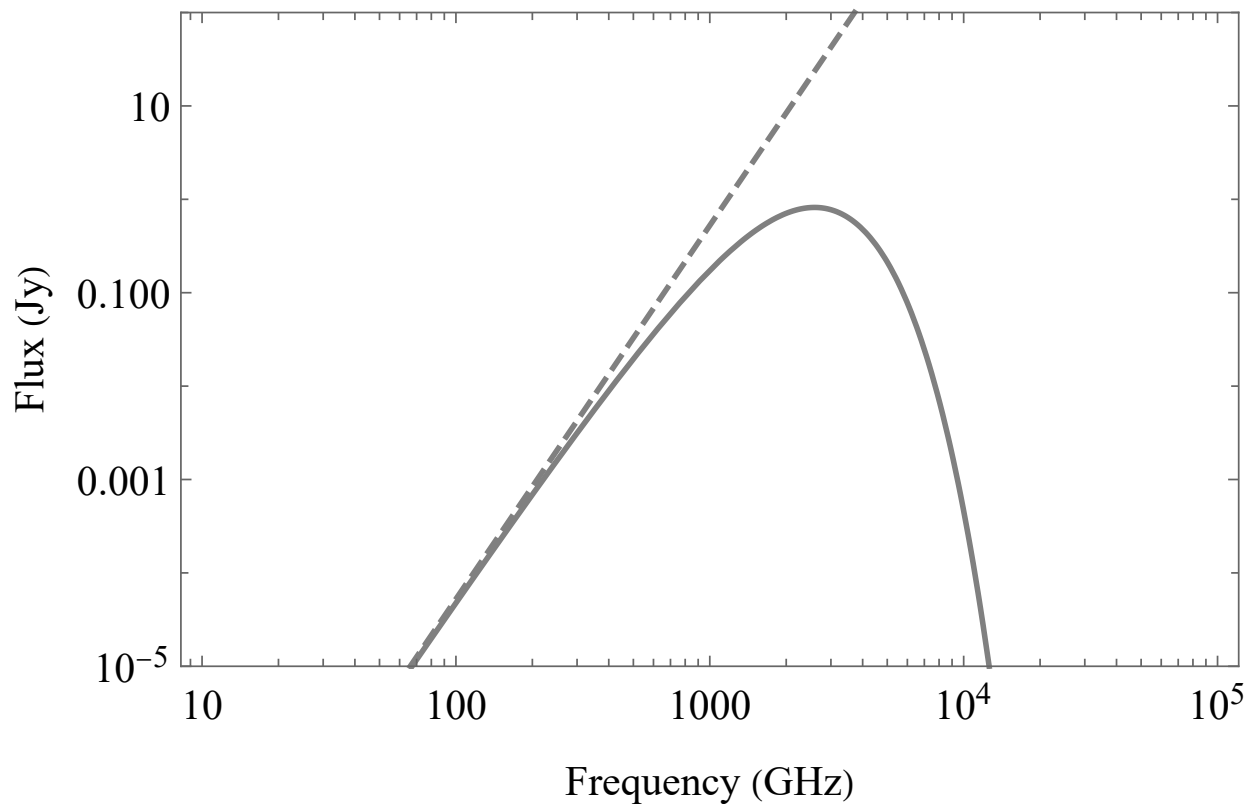
Figure 1.3 The solid line shows a modified blackbody curve for a theoretical galaxy at distance $D = 20\,\mathrm{Mpc}$ with $M_d = 5 \times 10^5\,M_\odot$, $T_d = 25\,\mathrm{K}$, and $\beta = 2.00$. The dashed line is the Rayleigh-Jeans approximation for the same theoretical galaxy.

us an anti-correlation [20, 21]. Additionally, the β we observe may be different from the intrinsic β of the dust [23]. Studies of interstellar dust clouds find that line-of-sight temperature variations cause negative correlation when dust is internally heated, but when dust is externally heated there is a positive correlation [24]. To recover the intrinsic β, the MBB must be constrained past 100 μm (lower than 3×10^{12} Hz) [25]. If data in only lower-frequency ranges falls prone to $T_d - \beta$ anti-correlations and data without low frequency points fails to recover the intrinsic β, it is important to have data at a large range of frequencies, both above and below the peak emission.

1.4   ALMA

The Atacama Large Millimeter/submillimeter Array (ALMA) is a telescope array of 66 radio telescopes in Chile. Through interferometry, or the extraction information from the interference of electromagnetic waves, ALMA acts as a single large telescope with a size equivalent to the area of the telescope array. This is useful because the size of telescopes directly affects how much information can be gathered. In the case of ALMA, the large size of the array allows high resolution imaging in the millimeter/submillimeter regime.

The high resolution of ALMA has enabled it to image CO emissions of CNDs in $\sim$100 ETGs. These data sets allow for detailed mapping of the molecular gas properties and kinematics of these disks. When these gas kinematics show circular rotation at low disk radii, the ALMA data can provide precision measurements of the supermassive black holes found at the center of these galaxies [26–29]. ALMA data is also used to determine gas cloud properties [30], star formation [31], and the feeding of active galactic nuclei [32]. However, only a fraction of ALMA data is being used for these projects, with many ALMA data sets left underutilized.

This thesis is the first step in preparing a census of gas and dust properties in ETGs using these data sets from the ALMA archive. With the high-resolution ALMA data sets, we can directly

image CNDs and obtain continuum flux measurements at 1.08, 2.36, and 3.49×10^{11} Hz. These frequencies are part of the Rayleigh-Jeans regime, and are therefore vital to accurately constraining β. Additionally, many ETGs experience contamination at these frequencies from active galactic nuclei (AGN) synchrotron emission. Thanks to the high-resolution of ALMA, we can model the AGN emission and subtract it from the total flux to isolate the thermal dust emission and bypass the contamination of these targets.

1.5   The Sample

This project focuses on accurately constraining the dust masses, temperatures, and emissivity indices of the CNDs of five ETGs from the ALMA imaging archive, namely NGC 1380, NGC 3557, NGC 4374, and NGC 6861. These galaxies have all been chosen for a number of different criteria to test the effectiveness of modeling their MBBs with ALMA data. While some of these galaxies have an abundance of data available at a large range of frequencies, some have very little data. While some have minimal AGN contamination, some galaxies are heavily contaminated. This diversity will help us know if our methods will be effective for a larger, more complete sample.

In Chapter 2 of this thesis, we aim to accurately model each galaxy with a MBB using a least-squares fitting function called `MPFIT`. We acquire uncertainties for our measured parameters with both frequentist and Bayesian analysis. We use the full-SED modeling code `CIGALE` to confirm the types of each emission and to compare results with MPFIT. We also use ALMA CO imaging to simulate mass and temperature gradients in the CND of NGC 6861, and test how these gradients affect the result of our MBB fits. Results are presented in Chapter 3. We list dust masses, temperatures, and emissivity slopes for each galaxy and state the corresponding uncertainties. We compare the dust masses found by `MPFIT` with the dust masses found by `CIGALE`. We discuss potential problems with our data sets. We also find that dust mass temperature gradients are

unnecessary for constraining accurate parameters.

Chapter 2

Methods

Our data collection and fitting techniques are presented in this chapter. In Section 2.1, we present the telescopes and surveys from which we gathered data. In Section 2.2, initial fitting and modeling techniques are describe. In Section 2.3, we describe use a full-SED modeling code. Finally, in Section 2.4, we discuss gas properties and methods for determining mass and temperature gradients.

2.1   Data

As discussed in Section 1.3, flux measurements are needed for frequencies both higher and lower than the peak blackbody emission. Ideally, we would thoroughly sample through the whole range of frequencies for which thermal dust emission is the primary emission detected from the ETG. However, we are dependent on archival data so we are limited by the sky coverage of previous surveys.

This project relies heavily on the mm/sub-mm wavelength data from ALMA, however, other telescopes are needed to fully flesh out the SED of the thermal dust emission. For this project, we used archival data from the Herschel Space Observatory, the Infrared Astronomical Satellite (IRAS), the Infrared Space Observatory (ISO), and the Spitzer Space Telescope. Unfortunately, synchrotron

radiation from a galaxy's AGN presents an obstacle when acquiring data. Flux measurements at lower frequencies can be contaminated with this synchrotron emission. In other words, both thermal and non-thermal emission are present in the measurement. With ALMA, the non-thermal emission is modeled and subtracted off of the image, but Herschel, the source of our other low-frequency data, does not have high enough resolution for the same method to work. Instead, the solution lies in modeling the synchrotron SED. Most of this emission is found in the radio regime, so we acquired archival data from the Mullard Radio Astronomy Observatory (MRAO), the Very Large Array (VLA), the Aricebo Observatory, the Green Bank Observatory, the National Radio Astronomy Observatory (NRAO), the Australia Telescope Compact Array (ATCA), the Parkes Observatory, and the Very Large Baseline Array (VLBA).

In Section 2.3, we model the SEDs of the galaxies in our sample from X-ray to radio, in addition to the IR-mm fitting for just the MBB emission. In addition to the previous telescopes, we acquired archival data in ultraviolet, optical, and infrared (UVOIR) wavelengths from the Wide-field Infrared Survey Explore (WISE), the Two Micron All-Sky Survey (2MASS), the Sloane Digital Sky Survey (SDSS), the La Silla Observatory, and the Galaxy Evolution Explorer (GALEX). We also acquired archival data in the X-ray regime from the Chandra X-ray Observatory. All flux measurements used in this thesis are listed in Table 2.1.

Table 2.1. Sample SED Measurements

Telescope (1)	Band / Filter (2)	$\log_{10}\nu$ (Hz) (3)	$\log_{10}\lambda$ (μm) (4)	NGC 1380 (5)	NGC 3557 (6)	NGC 4261 (7)	NGC 4374 (8)	NGC 6861 (9)
				in Jy units				
MRAO	Band S	9.43	5.05	...	...	...	3.953 (0.40)	...
	Band C	9.70	4.78	...	...	...	2.840 (0.29)	...
VLA	Band S	9.15	5.33	$[1.6\,(0.5)] \times 10^{-3}$	...	22.0 (1.0)	6.095 (0.122)	...
Arecibo	Band S	9.38	5.10		...	...	3.635 (0.146)	...
Green Banks	Band C	9.69	4.79	...	...	...	3.582 (0.537)	...
NRAO	Band X	10.03	4.47	...	...	5.00 (0.58)	...	...
				in mJy units				
	Band L/S	9.32	5.16	...	252 (25.2)	...	...	...
ATCA	Band C	9.68	4.80	...	77 (7.95)	...	...	...
	Band X	9.93	4.55	...	23 (3.25)	...	...	...
	Band K	10.30	4.18	...	52 (6.56)	...	...	...
Parkes	Band S	9.70	4.78	...	...	...	...	< 30
	Band C	9.70	4.78	2.1 (4.6)	...	...	...	20.0 (2.0)
	Band S	9.48	5.00	2.06 $\left(^{+0.23}_{-0.18}\right)$	9.86 $\left(^{+0.99}_{-0.79}\right)$	302.73 $\left(^{+24.44}_{-9.08}\right)$	114.95 (3.45)	...
	Band C	9.69	4.79	...	...	...	168.7 (4.2)	...
VLA (S_{nuc})	Band C	9.92	4.55	...	...	...	163.1 (4.1)	...

Table 2.1 (cont'd)

Telescope (1)	Band / Filter (2)	$\log_{10}\nu$ (Hz) (3)	$\log_{10}\lambda$ (μm) (4)	NGC 1380 (5)	NGC 3557 (6)	NGC 4261 (7)	NGC 4374 (8)	NGC 6861 (9)
	Band Ku	10.18	4.30	...	...	...	165.3 (4.1)	...
	Band Ku	10.18	4.30	...	...	300 (7.5)	180.7 (4.7)	...
VLBI (S_{nuc})	Band C	9.69	4.79	...	...	390 (39)	186 (19)	...
ALMA (S_{nuc})	Band 3	11.03	3.45	4.18 (0.42)	23.70 (2.40)	...	99.66 (10.0)	...
	Band 6	11.37	3.11	6.05 ($^{+0.64}_{-1.14}$)	15.5 (1.55)	251.9 (25.2)	126.0 ($^{+13.1}_{-16.1}$)	22.6 (2.29)
	Band 7	11.54	2.94	...	...	224 (22.4)	134.2 (20.13)	15.8 (1.6)
ALMA (S_{disk})	Band 3	11.03	3.45	0.21 (0.09)	...	...	...	...
	Band 6	11.37	3.11	2.35 ($^{+0.67}_{-0.40}$)	0.96 ($^{+0.31}_{-0.96}$)	0.17 (0.02)	1.31 ($\pm$0.88)	< 2.04
	Band 7	11.54	2.94	...	...	0.72 (0.20)	...	2.9 (0.29)
Herschel SPIRE		11.78	2.70	138 (17.8)	...	234 (41.1)	118 (16.1)	...
		11.93	2.55	372 (50.0)	81.7 (10.9)	238 (59.9)	208 (25.1)	...
		12.08	2.40	1080 (128)	133 (14.3)	207 (42.6)	249 (28.5)	...
Herschel PACS		12.27	2.21	2140 (264)	...	232 (68.2)	597 (41.8)	...
		12.48	2.00	2840 (244)	...	243 (71.4)	963 (119)	...
		12.63	1.85	...	...	...	...	...
IRAS		12.50	1.98	3125 (219)	...	150 (49)	980 (216)	3068 (337)
		12.76	1.72	1083 (65)	...	80 (35)	502 (55)	842 (101)

Table 2.1 (cont'd)

Telescope (1)	Band / Filter (2)	$\log_{10} \nu$ (Hz) (3)	$\log_{10} \lambda$ (μm) (4)	NGC 1380 (5)	NGC 3557 (6)	NGC 4261 (7)	NGC 4374 (8)	NGC 6861 (9)
ISO	ISOCAM	12.18	2.29	⋯	⋯	310 (100)	490 (120)	⋯
		12.24	2.24	⋯	⋯	390 (110)	710 (130)	⋯
		12.56	1.91	⋯	380 (90)	160 (80)	660 (110)	⋯
		12.72	1.76	⋯	290 (100)	70 (80)	410 (90)	⋯
Spitzer	MIPS	12.29	2.18	⋯	271 (28)	375 (18)	535 (61))	⋯
		12.64	1.84	⋯	276 (19)	127 (11)	617 (41)	⋯
		13.11	1.37	⋯	30.6 (4.5)	51.5 (3.2)	66.6 (8.6)	⋯
WISE	W4	13.13	1.35	122 (7.90)	32.4 (3.78)	113 (10.1)	135 (15.1)	87.6 (6.98)
	W3	13.41	1.07	162 (11.7)	74.5 (8.14)	104 (8.54)	261 (99.6)	95.1 (5.02)
	W2	13.81	0.67	380 (21.0)	331 (9.46)	399 (11.6)	1080 (117)	219 (11.0)
	W1	13.95	0.53	777 (36.8)	618 (14.8)	670 (16.1)	1490 (224)	372 (18.7)
Spitzer	IRAC2	13.83	0.65	364 (36.4)	⋯	371 (37.1)	714 (71.4)	211 (21.1)
	IRAC1	13.93	0.55	585 (58.5)	539 (53.9)	452 (45.2)	1240 (124)	297 (29.7)
2MASS	K	14.14	0.34	1480 (38.2)	1020 (26.3)	1050 (27.1)	2870 (74.1)	655 (16.9)
	H	14.26	0.22	1670 (43.1)	1260 (32.5)	1250 (32.3)	3440 (88.8)	816 (21.1)
	J	14.39	0.09	1410 (34.4)	1050 (25.6)	997 (24.3)	2740 (66.8)	671 (16.4)
SDSS	z	14.53	−0.05	⋯	⋯	638 (31.9)	2060 (103)	⋯

2.2   MPFIT

For the initial MBB fitting process, we optimized the SED model using `MPFIT`, a least-squares fitting function [33]. Before inputting the data, it was necessary to first account for any emission that was not thermal dust emission. To account for the possible contamination from AGN synchrotron emission and stellar emission, we fit power-laws of the form

$$S_\nu = S_0 \left(\frac{\nu}{1 \, \text{GHz}} \right)^\alpha. \tag{2.1}$$

Here, S_ν is the measured flux from the AGN or stellar emission, ν is the frequency in Hz, α is the power-law slope (usually ~ -0.7 for synchrotron emission and ~ 2 for stellar emission), and S_0 is the flux at 1 GHz. From the radio data, we fit Equation 2.1 to find values of $S_{0,\text{rad}}$ and α_{rad}, and from the WISE and mid-infrared Spitzer data we fit Equation 2.1 to find values of $S_{0,\text{stel}}$ and α_{stel}. The resulting radio and stellar flux power-laws were then subtracted from the Herschel, IRAS, ISO, and far-infrared Spitzer flux measurements. This subtraction is unnecessary for ALMA as the non-thermal emission had already been modeled off of the image in the ALMA S_{disk} values. We input all the resulting data where 10^{11} Hz$< \nu < 10^{13}$ Hz into `MPFIT`, which fit Equation 1.1 and output M_d, T_d, and β for each galaxy.

2.2.1   Uncertainty Analysis

We obtained formal uncertainties for our parameters M_d, T_d, and β in two ways. The first was through the use of a frequentist Monte Carlo resampling. The process for Monte Carlo resampling is as follows: for each galaxy, we took its fitted MBB model and created artificial noise by taking S_ν at each frequency for which we had photometry and adding a random value from a normal distribution centered at zero. The standard deviation of the distribution was set to the error for the original data at that frequency. We then ran `MPFIT` with these new artificial flux values. This process was repeated for 500 iterations. We set our formal uncertainties of each parameter M_d, T_d, and β to the

Table 2.1 (cont'd)

Telescope (1)	Band / Filter (2)	$\log_{10} \nu$ (Hz) (3)	$\log_{10} \lambda$ (μm) (4)	NGC 1380 (5)	NGC 3557 (6)	NGC 4261 (7)	NGC 4374 (8)	NGC 6861 (9)
	i	14.60	−0.12	⋯	⋯	504 (24.2)	1530 (73.6)	⋯
	r	14.69	−0.21	⋯	⋯	352 (16.9)	1020 (49.2)	⋯
	g	14.81	−0.33	⋯	⋯	160 (7.70)	508 (24.4)	⋯
	u	14.92	−0.44	⋯	⋯	33.5 (1.84)	72.6 (4.00)	⋯
La Silla ESO	R	14.67	−0.19	477 (41.2)	297 (25.7)	⋯	⋯	176 (15.2)
	B	14.82	−0.34	158 (13.6)	80.7 (6.97)	⋯	⋯	54.0 (4.67)
GALEX	NUV	15.12	−0.64	2.61 (0.32)	0.97 (0.10)	1.76 (0.20)	4.05 (0.43)	1.11 (0.12)
	FUV	15.29	−0.81	0.66 (0.07)	0.17 (0.02)	0.60 (0.07)	1.17 (0.13)	0.508 (0.06)
in nJy units								
Chandra (S_{nuc})	0.3–8 keV	18.00	−3.52	7.97 $\left(^{+0.44}_{-1.14}\right)$	32.0 $\left(^{+14.0}_{-3.0}\right)$	48.1 $\left(^{+4.2}_{-0.5}\right)$	38.3 $\left(^{+6.5}_{-0.7}\right)$	23.8 $\left(^{+0.7}_{-14.2}\right)$

Note. — Cols. (5) through (9) give flux densities integrated over respective emission region for this sample of ETGs, in either Jy, mJy, or nJy units as indicated above each section. Cols. (1) and (2) give the telescopes and instruments/bandpasses. Nuclear flux densities (S_{nuc}) were estimated by the peak flux values, whereas locally extended continua ($_{\mathrm{disk}}$) were integrated over the entire dusty disk region. Cols. (3) and (4) report the frequency and effective wavelengths.

standard deviation of each of the respective sets of new values.

Our second set of uncertainties were obtained through Bayesian analysis using the MCMC code from the `emcee` package for `python` [34]. We input our `MPFIT` values of M_d, T_d, and β as priors for our algorithm. We again used Equation 1.1 along with flux measurements with stellar and synchrotron power-laws subtracted off. We ran `emcee` with 200 walkers for 1000 iterations, with a burn-in of 500 iterations. The logarithmic-likelihood function used by the walkers was:

$$\chi^2 = -\frac{1}{2}\sum\left(\frac{S_{\nu\mathbf{data}}-S_{\nu\mathbf{model}}}{S_{\nu\mathbf{data,err}}}\right)^2. \tag{2.2}$$

The walkers appeared to converge within the 1000 iterations. Standard deviations for each parameter were drawn from the final iteration of the walkers and used as our second formal uncertainty. We see close agreement ($\lesssim 10\%$ differences) between the two methods of uncertainties.

2.3   CIGALE

In Section 2.2, we made the assumption that all non-thermal emission could be modeled with a set of power-law functions. However, running a full SED analysis using robust software could model all sources of emission. This would help us confirm that we are modeling thermal dust emission with MPFIT, and would also produce comparison values for our parameters. To perform this task we used `CIGALE`, an SED modeling code [35–37]. `CIGALE` runs with several modules that model properties such as star formation rates and total dust luminosity. Each module requires several user-input parameters, from which it builds a grid of models. `CIGALE` can then determine the best fit properties of a galaxy using Bayesian analysis and the best fit input parameters by examining the likelihood of each model.

To model our star formation rate (SFR), we used the `sfhdelayed` module, which assumes a steady increase in the SFR before the peak and an exponential decrease afterwards. Our stellar population was modeled with the `bc03` module, which uses the single stellar population library

of Bruzual & Charlot (2003) [38]. For this module we assumed a standard metallicity of 0.02, a separation age between the old and young stellar populations of 10 Myr, and the initial mass function from Chabrier (2003) [39].

Modeling the dust attenuation is vital to maintaining the energy balance principles that `CIGALE` utilizes. Light absorbed by dust at UVOIR wavelengths is re-emitted in the mid to far-IR. We used the empirical `dustatt_modified_starburst` module to model how much light is absorbed by the dust. To model how light is emitted by the dust, we used the `dl2014` module, which is based off of the modeling techniques put forth by Draine & Li (2007) [40] and reworked by Draine et al. (2014) [41].

Knowing the AGN contribution to these SEDs is important in determining how much mid to far-IR emission is thermal emission from dust, as AGN emission can contaminate the mid to far-IR range. To determine AGN emission, we used the `skirtor2016` module, which is based off of the SKIRTOR model [42, 43]. To model X-ray emission, we used the `xray` module, and we used the `radio` module to model radio emission. These modules model X-ray and radio emission from both AGN and non-AGN sources.

Each module in `CIGALE` computes its respective portion of the SED based on the parameters that are input by the user. If desired, several options can be input for each parameter. In this case, `CIGALE` runs each possible model built from the input parameters and chooses the one with the best likelihood. Many of the properties we are trying to extract with `CIGALE` are in the form of input parameters and not fitted variables, so our grid of input parameters can quickly become large. To compensate for computational limitations, we focused on finding satisfactory inputs for one module at a time. For each module, we input a large range of numbers for each parameter. After running `CIGALE` and finding the best fit parameters, we repeated the process as needed with the parameter ranges closing in more tightly on better fitting values. When a module was finished, we allowed the parameters for that module to vary slightly when fitting the parameters of the next module

to account for possible degeneracies between separate modules. This process allowed us to have reasonable computation times for `CIGALE` while also giving precise parameters.

A drawback of `CIGALE` is that only global flux data can be fit. ALMA S_{disk} values could not be fit alongside ALMA S_{nuc} values (peak emission without source subtraction) or radio values. To compensate, we fit each galaxy twice. The first fit, our main fit, uses all the global data from radio to X-ray, while the second fit does not fit to radio points but fits to ALMA S_{disk} points. The first method can be used to determine the influence of AGN emission in our fit, while the second method can better constrain dust parameters using ALMA S_{disk} data. As with `MPFIT`, when fitting without the radio data, we subtracted the synchrotron power-laws described in Section 2.2 off of the mid to far-IR data before fitting to ensure we only fit to dust emission.

2.4   Gas Masses and CND Mass and Temperature Gradients

Detection of gas is often done by detecting emission lines, or light emitted at specific frequencies. These frequencies depend on quantized energy transitions in the gas molecule or atom. In CO, emission lines can be made in the sub-mm to mm regime because of rotational transitions, i.e. a CO molecule changes its rotational mode due to processes such as collisions. Through imaging CO transition lines with ALMA, a variety of gas properties can be recovered. Arguably the simplest of these recoverable properties is the gas mass, as gas mass is roughly proportional to the luminosity of the CO emission line. We can also find the temperature of the disk, although this is a more involved process. Because of ALMA's high resolution, we can find mass and temperature gradients for the CND. Applying these gradients to our MBB can demonstrate the differences between a single temperature fit and a gradient temperature fit. For the gradient fit, we divide the CND into 10 annuli. We assign each annulus a temperature and a mass as determined by the gradients and find the blackbody emission S_ν of the annulus. Summing the emission of all the annuli together

gives us an SED model that we can compare to the MPFIT model. We simulate gradients for NGC 6861 because of the quality ALMA CO imaging available. These gradients could be recovered from ALMA continuum images (the images used to derive flux values of MBB emission), however, the CO transition line images available are higher quality.

2.4.1 Gas Mass and Mass Density

To determine the CO luminosity from the flux of the CO(1−0) emission line (representing the transition from the first excited rotational mode to the ground state), we use the equation

$$L'_{CO} = 3.25 \times 10^7 I_{CO} \Delta v \frac{D_L^2}{(1+z)^3 v_{obs}^2} \text{K km s}^{-1} \text{pc}^2, \tag{2.3}$$

where $I_{CO} \Delta v$ is the CO(1−0) line intensity in Jy km s^{-1}, D_L is the luminosity distance in Mpc (1 Mpc = 10^6 pc), and v_{obs} is the observed frequency in GHz [44]. CO luminosity is related to H$_2$ mass by $M_{H_2} = \alpha_{CO} L'_{CO}$. Using a helium mass fraction of $f_{He} = 0.36$, we estimate the total gas mass to be $M_{gas} = M_{H_2}(1 + f_{He})$. We adopted the ratios $R_{21} = I_{CO(2-1)}/I_{CO(1-0)} \approx 0.7$ and $\alpha_{CO} = 3.1 \, M_\odot$ pc^{-2} (K km s^{-1})$^{-1}$ from averages of a sample of nearby of late-type galaxies [45]. Measurements for the $I_{CO(2-1)}$ values of NGC 1380, NGC 4261, NGC 4374, and NGC 6861 were reported by Boizelle et al. (2017) [14] and Boizelle et al. (2021) [29]. Using the same process, we found the integrated CO(2−1) flux of NGC 3557.

Boizelle et al. (2017) [14] show I_{CO} vs radius for a number of ETGs, including NGC 6861. Using the above relationships, we can take I_{CO} as a proxy for the surface mass density of the disk. If we assume a well mixed ISM, i.e. if there is a constant proportion of gas to dust throughout the disk, this surface mass density can be adapted for both the gas mass density and the dust mass density of the disk. To do this, we first define $I(r)$ to be I_{CO} at radius r. We then define a to be the proportionality constant between intensity and mass density. To find a, we take our total derived dust mass (found from `MPFIT` or from the methods described earlier in this section) and divide by

intensity integrated over the disk:

$$a = M / \int_{\text{disk}} I(r) r dr d\phi. \tag{2.4}$$

Then we can represent the surface mass density as

$$\Sigma(r) = aI(r) = \frac{MI(r)}{\int_{\text{disk}} I(r) r dr d\phi}. \tag{2.5}$$

See Fig. 2.1 for the surface mass density of NGC 6861's dust content.

2.4.2   Gas Temperature

ALMA has both $CO(2-1)$ and $CO(3-2)$ data available for NGC 6861. By overlaying the two CO flux maps, we can get the line intensity ratio $R_{32} = I_{CO(3-2)}/I_{CO(2-1)}$ at each pixel of our image. Assuming similar H_2 number densities (number of H_2 molecules per volume) and CO column densities (the amount of CO molecules in our line of sight per area on the CND), R_{32} can give us the temperature of the disk at different locations. Using the online RADEX modeling program [46], we assumed H_2 number densities, and CO column densities to convert R_{32} to temperatures. We acquired temperatures for 3 regions: the inner disk, the outer disk, and external clumps. From these three temperatures, we found that temperature was roughly linear with radius and fit a simple line to the data (see Fig. 2.1). An H_2 number density of 10^4 cm^{-3} and a CO column density value of $10^1 5$ cm^{-2} were chosen such that inputting the temperature gradient into the MBBs of each of the 10 annuli resulted in a peak of the superposed emission curve at similar frequencies to the peak seen in the MPFIT models. Because the peak of a blackbody curve is dependent on temperature, we know that the temperature of the CND must be fit in such a way that the peaks match. This again assumes a well mixed dust and gas reservoir, such that the temperatures of the gas and dust are equal. Given the data available, there is no other obvious way to determine gas temperature than through comparing the superposed SED to the MPFIT model.
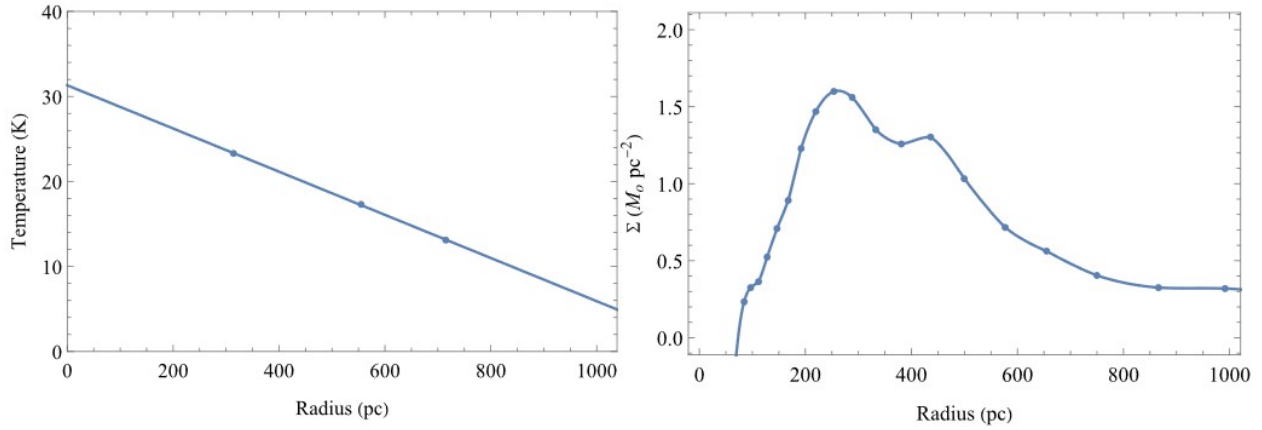
Figure 2.1 Left Panel: Estimated CND temperature gradient based off CO emission line ratios. Right Panel: Estimated dust mass gradient based off CO emission line intensities.

2.4.3   Simulated SED

With a mass gradient derived from CO emission intensity and a linear temperature gradient, a simulation of NGC 6861's SED can proceed. What this simulation aims to do is to see how closely MPFIT can recover the same M_d and β values with gradient mass and temperature compared to with single mass and temperature values.

As described above, this simulation assumes the CND can be split into 10 annuli with differing mass and temperatures. The thermal dust emission of this CND would be given by

$$S_\nu = \sum_{i=1}^{10} S_{\nu,i} \tag{2.6}$$

Where S_ν, i is given by inputting $M_{d,i}$, $T_{d,i}$, and β into Equation 1.1. $M_{d,i}$ is found by integrating $\Sigma(r)$ from Equation 2.5 over annulus i and $T_{d,i}$ is found by evaluating the linear temperature−radius relation at the average radius of the annulus. Because $\Sigma(r)$ is dependent on M_d, both M_d and β are free variables in this simulated SED. We input Equation 2.6 into MPFIT to recover M_d and β for this model.

Chapter 3

Results

In this chapter, we present results of our SED fitting runs for both `MPFIT` and `CIGALE` in Sections 3.1 and 3.2 respectively. We present discussion on the effectiveness of a mass and temperature gradient in Section 3.3. In Section 3.4, we present our results and conclusions.

3.1 MPFIT Results

We have found values and uncertainties for M_d, T_d, and β through `MPFIT` fitting and through frequentist and Bayesian analysis. These are listed in Table 3.1, along with gas masses M_{gas} derived using the methods described in Section 2.4.1. Also listed are `MPFIT` results where β was fixed to 2.00. This is done to compare to previous works such as Smith et al. (2012), di Serego Alighieri et al. (2013), and Kokusho et al. (2019) [6–8]. Corresponding SEDs as fit by `MPFIT` are shown in Fig. 3.1.

We find with a free β parameter that values of M_d range from $(1.9-21.1) \times 10^5 \ M_\odot$, with an average M_d of $10.1 \times 10^5 \ M_\odot$. T_d ranges from 18.1 to 36.4 K with an average of 26.7 K. We find β ranging from 1.22 to 3.29 with an average of 2.25. When we fix β to 2.00, we find a lower average M_d of $6.0 \times 10^5 \ M_\odot$, with values ranging from $(2.0-10.6) \times 10^5 \ M_\odot$. This is mostly due to the

Table 3.1.   Galaxy Gas and Dust Parameters

Galaxy (1)	$I_{CO(2-1)}$ (Jy km s^{-1}) (2)	M_{gas} ($10^7 M_\odot$) (3)	M_d ($10^5 M_\odot$) (4)	M_{gas}/M_d (5)	T_d (K) (6)	β (7)
NGC 1380	78.35	8.4 (1.6)	11.1 (1.1/1.0)	76	26.1 (0.8/0.7)	2.08 (0.11/0.10)
			10.6 (0.9/0.9)	79	26.7 (0.3/0.4)	2.00 (−)
NGC 3557	7.09	5.4 (0.5)	7.9 (1.0/1.0)	76	31.6 (1.7/1.5)	1.42 (0.14/0.13)
			9.2 (1.0/1.1)	58	27.0 (0.6/0.6)	2.00 (−)
NGC 4261	3.06	1.1 (0.2)	8.6 (1.1/1.2)	13	18.1 (0.8/0.8)	3.23 (0.28/0.25)
			4.1 (0.5/0.4)	28	24.7 (0.5/0.4)	2.00 (−)
NGC 4374	4.81	0.57 (0.10)	1.9 (0.2/0.2)	31	36.4 (2.1/2.1)	1.22 (0.18/0.17)
			2.0 (0.2/0.2)	29	29.4 (0.6/0.6)	2.00 (−)
NGC 6861	93.93	25.6 (8.9)	21.1 (5.6/5.7)	121	21.3 (1.3/1.3)	3.29 (0.19/0.21)
			3.9 (0.4/0.4)	656	33.4 (0.8/0.7)	2.00 (−)

Note. — Col. (2): The CO(2−1) flux integrated over the dusty disks. Col. (3): Gas mass derived from CO(2−1) flux. Cols. (4), (6), (7): Cold dust mass (M_d), temperature (T_d), and emissivity slope (β) derived from a modified blackbody fit to thermal emissions in the mid to far-IR. Upper values are results from runs with a free β parameter, and lower values are from runs where β is fixed to 2.00. Values found in the parenthesis are the uncertainties from frequentist analysis and from Bayesian analysis respectively. Col. (5): Gas mass/dust mass ratio.
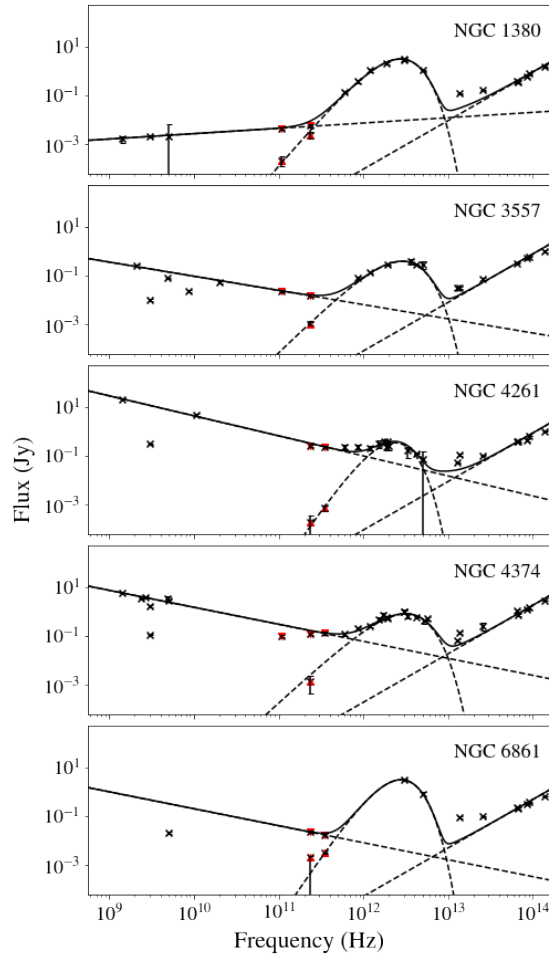
Figure 3.1 SEDs in the radio and mid to far-IR range are shown for each galaxy. The thermal emission, along with our best fit modified blackbody, can be seen between $\sim 10^{11}$ and 10^{13} Hz in each galaxy. Also seen are power laws representing stellar emissions and radio emissions. Red up-pointing triangles represent ALMA extended data and red down-pointing triangles are represent ALMA nuclear data.

vastly different M_d values for NGC 6861. We find a higher average T_d of 28.2 K with a smaller range of 24.7 to 33.4 K. Comparing these values from the $\beta = 2.00$ fits with those of Smith et al. (2012) and Kokusho et al. (2019) [6, 8], we see that our sample of galaxies is somewhat of an average sample, with M_d and T_d lying well within the ranges of these two surveys. Note that these

two samples were not explicitly designed to measure the dust content of CNDs and galaxies with less regular dust features may be included. We expect many, if not most, ETGs with significant dust populations to house their dust in CNDs. There may be some galaxies with dust beyond their CNDs or galaxies with no CNDs at all, yet the majority of their respective samples are expected to be comparable to the galaxies in our sample. See Fig. 3.2 for histograms comparing our sample to the previously mentioned samples.
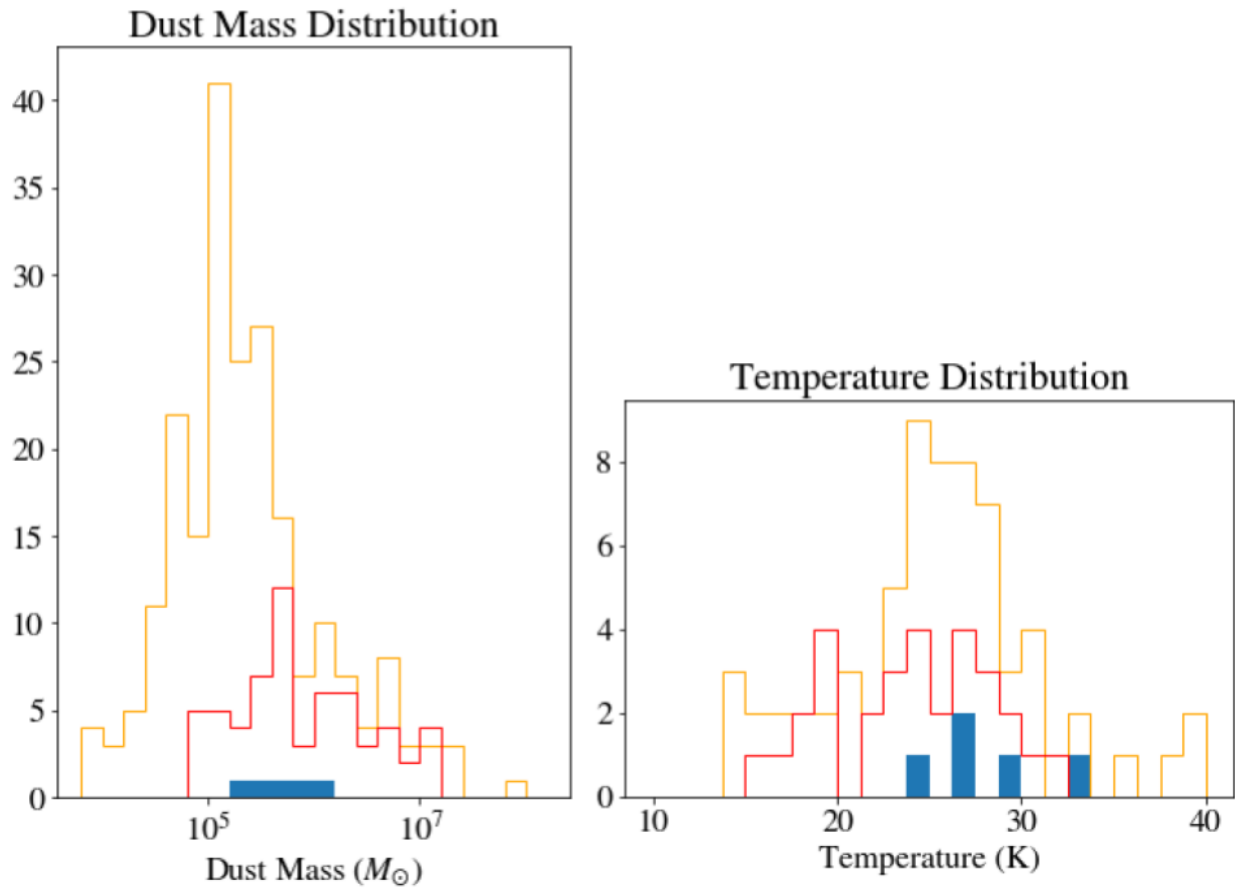
Figure 3.2 In this figure, our sample (blue) is compared to samples from Smith et al. (2012) [6] in red and Kokusho et al. (2019) [8] in orange. Dust masses form the *x*-axis on the left and dust temperatures form the *x*-axis on the right, with number of galaxies being the y-axis in both cases.

The average uncertainties for M_d, T_d, and β are 14.6%, 4.7%, and 8.4% respectively. The largest uncertainty for T_d is only 6.1%, while M_d and β both have higher uncertainties. The largest uncertainty for M_d is 27.0% for NGC 6861. This galaxy also has the highest β ($\beta = 3.29$) and only three useful photometric data points in the mid-IR to microwave range (the ALMA band 6 extended measurement is only an upper limit), so more data points could help us better constrain the properties for this galaxy. The largest uncertainty for β is 13.9% for NGC 4374. The far-IR data for this galaxy seem to be polluted by a radio power-law, so we rely on a subtraction of the synchrotron power-law from far-IR data and a single ALMA extended data point with a >200% upper uncertainty to see the Rayleigh-Jeans tail of the thermal dust emission. Additional information regarding the uncertainty of these parameters can be found in Appendix A, where we show and discuss corner plots (plots showing degeneracies and parameter uncertainties) from `emcee`.

3.2 CIGALE Results

Though `CIGALE` is a robust and versatile program, we aim to use `CIGALE` only for its ability to examine the dust populations in each galaxy with respect to other sources of emission. To accomplish, we found the dust luminosity L_d, the dust mass M_d, the stellar mass M_{stel}, and the AGN luminosity L_{AGN} for each galaxy using `CIGALE`. These values can be found in Table 3.2, with corresponding SEDs found in Fig. 3.3.

We find that for most parameters, there is little difference between the values for when radio data was fit to when the radio points were ignored. M_{stel} remains essentially unchanged, only NGC 4261 and NGC 6861 saw significant changes in L_d, and M_d was consistent for NGC 3557 and NGC 4374. NGC 1380 and NGC 6861 had moderate changes in M_d, but neither had changes as significant as NGC 4261. NGC 4261 has heavy AGN contamination, so fitting with the `radio` module fails to correctly model the Rayleigh-Jeans tail of the dust emission. Additionally, NGC 4261's high β

Table 3.2.   `CIGALE` Output

Galaxy (1)	M_{stel} $(10^9\ M_\odot)$ (2)	L_d $(10^9\ L_\odot)$ (3)	M_d $(10^5\ M_\odot)$ (4)	L_{AGN} $(L_d + L_{AGN})$ (5)
NGC 1380	89.6 (4.5)	1.13 (0.06)	9.7 (0.5)	0.1
	90.8 (4.5)	1.15 (0.06)	6.4 (0.7)	$(-)$
NGC 3557	276.3 (13.8)	0.88 (0.04)	11.8 (0.6)	0.3
	204.0 (10.2)	0.95 (0.15)	12.6 (1.5)	$(-)$
NGC 4261	225.0 (11.3)	0.38 (0.02)	25.5 (7.5)	0.8
	228.0 (11.4)	0.11 (0.02)	1.2 (0.2)	$(-)$
NGC 4374	167.0 (14.4)	0.34 (0.02)	2.8 (0.2)	0.4
	174.0 (14.9)	0.35 (0.02)	2.9 (0.1)	$(-)$
NGC 6861	110.5 (5.5)	2.12 (0.11)	10.4 (0.5)	0.1
	113.3 (5.8)	1.22 (0.29)	6.0 (1.4)	$(-)$

Note. — Upper values are `CIGALE` outputs from runs with the `radio` module, while lower values are outputs from runs without the `radio` module. Col. (2) lists the stellar masses of each galaxy. Col. (3) lists the dust luminosity of each galaxy. Col. (4) lists the dust mass of each galaxy. Col. (5) lists the AGN luminosity of each galaxy, represented as a fraction of the combined AGN and dust luminosity.
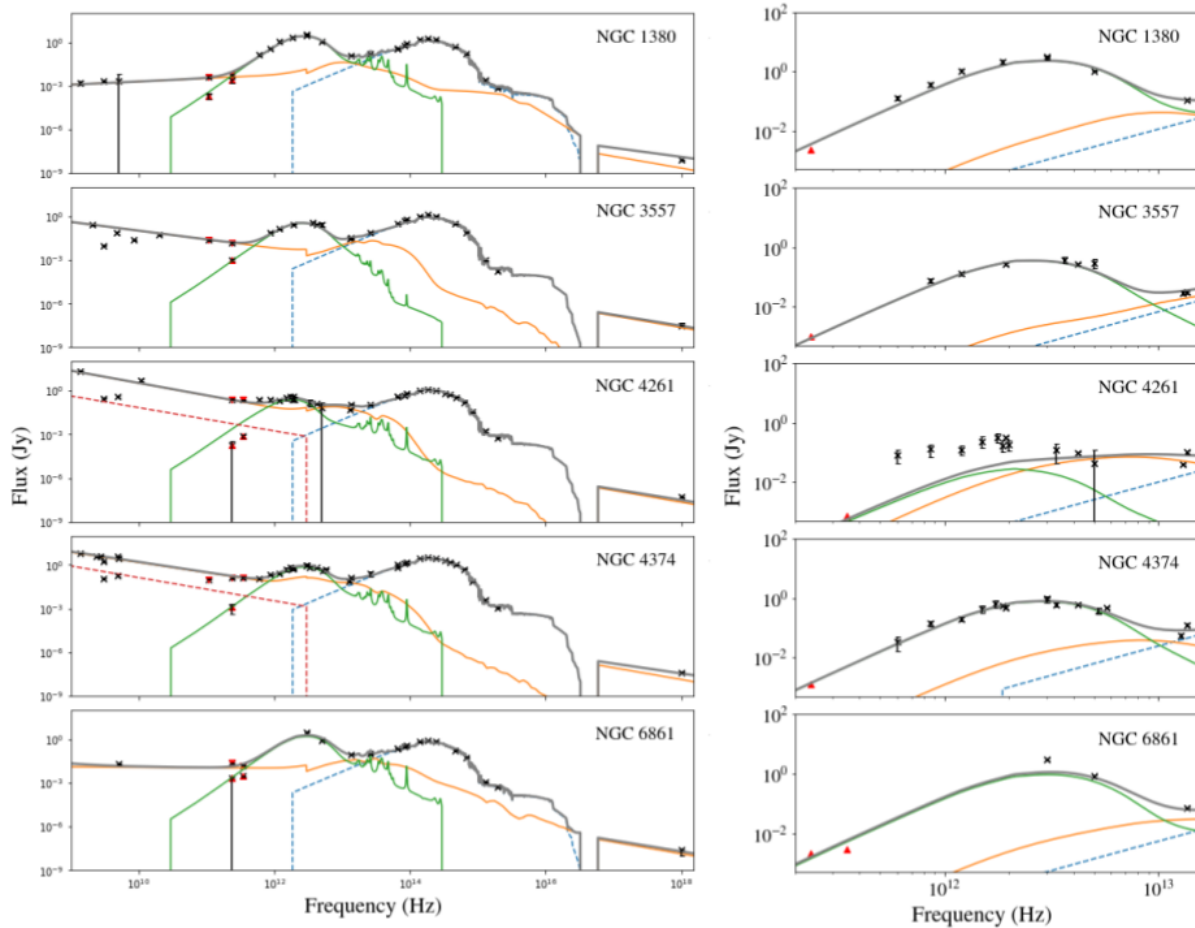
Figure 3.3 Left Panels: `CIGALE`-computed SEDs fit with the `radio` module from X-ray to radio. Right Panels: `CIGALE`-computed SEDs fit without the `radio` module in the mid to far-IR range are shown for each galaxy. Both Panels: The dashed blue represents stellar emission, green represents dust emission, orange represents AGN emission, and red represents radio emission from star formation. The solid gray is the total flux from the galaxy. Red up-pointing triangles represent ALMA extended data and red down-pointing triangles are ALMA nuclear data points.

prevents a good fit with the `radio` module off, as the `dl2014` module cannot account for the steep decline from the Herschel SPIRE data to the ALMA data.

   An important result from the `CIGALE` data is that our assumption of the AGN and stellar emission

modeled as a power-law seems justified. We see little trace of non-thermal dust emission that would be unaccounted for in power-law subtraction, with a possible exception being found in the high luminosity AGN emission of NGC 4261. However, we have already discussed the difficulty of fitting NGC 4261 with `CIGALE`.

3.3   Mass and Temperature Gradient Effectiveness

Using mass and temperature gradients to model NGC 6861 has shown interesting results. `MPFIT` fitting has determined M_d for NGC 6861 of $24 \times 10^5 \ M_\odot$, which is within the uncertainty limits of the isothermal M_d listed in Table 3.1. This method also gives a β of 3.08, which is just at the edge of the corresponding isothermal uncertainties. The temperature was not fit in this approach, as we determined a temperature gradient from CO line intensity ratios. An SED of the isothermal and temperature gradient fits is found in Fig. 3.4

The combination of output parameters and visual comparison reveal that the isothermal fit and temperature gradient fit give similar results. For this reason, we conclude that finding a mass and temperature gradient is unnecessary for the purpose of finding total mass and emissivity, at least to the current level of precision. We find that the temperature fit by the isothermal MBB method is warmer than the mass-weighted mean temperature of the disk and may represent a luminosity weighted temperature instead, i.e. the temperature fit by the MBB is the temperature of the annulus that produces the most emission. Additionally, we acknowledge the lack of data available in the far-IR for an SED fit of NGC 6861, and that additional data may change our conclusion.

3.4   Discussion and Conclusion

Analyzing these galaxies with both `MPFIT` and `CIGALE` gives an interesting perspective into these galaxies. `CIGALE` has the potential for a more detailed analysis, yet it requires more data across a
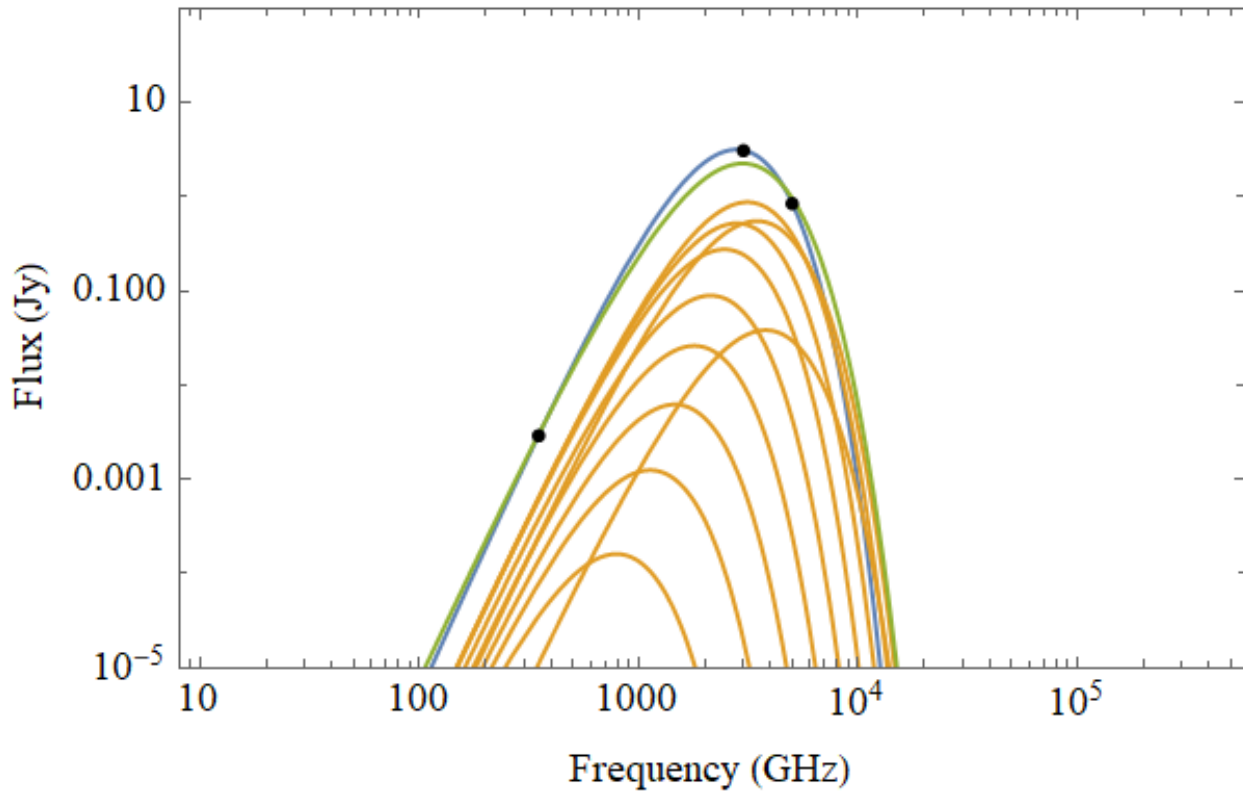
Figure 3.4 Dust emission of NGC 6861 as determined by both isothermal fitting and by temperature gradient fitting. The blue line represents dust emission as modeled by `MPFIT` from a single temperature fit. The green line represents dust emission as modeled by `MPFIT` by a temperature gradient fit, where the CND is split into 10 annuli and each annulus is assigned a mass and temperature. The orange lines represent the respective MBB emission of each annulus.

larger range of frequencies. `MPFIT` is simpler, though detail about non-thermal emission is lost and we are left to make assumptions about the emission we detect.

We see interesting results when examining M_d, T_d, and L_d for each galaxy. A comparison between the dust masses measured by these two methods show that NGC 1380 has a lower mass as measured by `CIGALE` than by `MPFIT`, yet the luminosity of the dust is higher for NGC 1380 then for NGC 3557, a galaxy with a higher dust content. `CIGALE` does not measure the dust luminosity

through mid-IR to mm emission, but rather by estimating the light attenuated by dust from stellar UVOIR emission. The higher luminosity of NGC 1380 would suggest higher temperatures to account for the lower dust mass, as $L \propto T^4$ by the Stefan-Boltzmann Law. However, we see lower temperatures for NGC 1380 than for NGC 3557, as evidence both by `MPFIT` output and by the position of the MBB peak in the respective SEDs. This would suggest that the `MPFIT` model of M_d is more correct in these cases, as the higher mass predicted by `MPFIT` would better explain the values of L_d and T_d we see for NGC 1380 and NGC 3557.

Many discrepancies we see between the masses fit by the two models may come down to the Rayleigh-Jeans regime. As we saw with the temperature and mass gradient fit, the emission is not strictly mass weighted or temperature weighted but rather depends on both. However, as luminosity goes as T_d^4, temperature can often be most important. When considering a situation like NGC 6861 where temperature is linearly related to radius, the hottest, most luminous parts of the CND are close to the center while most of the mass of the disk is cooler. This cool mass emits at lower frequencies where emission is largely dependent on β. Thus, carefully accounting for ALMA data is not only important for determining β but also for constraining dust mass.

This thesis provides the necessary first step for utilizing ALMA for larger scale studies of ETGs. Fitting MBB models with `MPFIT` proves to be a straightforward way to model dust emission in ETGs. ALMA S_{disk} values allow for more detailed analysis of β even in galaxies with high contamination from synchrotron sources. Although the MBB is an isothermal model, β and M_d are still well fit. Even T_d can provide insightful views of the temperature distribution of the disk. Future studies of CND temperature gradients may show that most of these gradients are linear as found in our study. If these studies find the slopes of these gradients are similar from disk to disk, an isothermal model like the MBB may be sufficient for most purposes. Even if such convenient trends are not found, isothermal T_d fits still represent the behavior of inner CND dust populations and can be used to study the star formation rates and the AGN effects on the ISM. To further constrain dust properties,

more observations are needed, especially in the Rayleigh-Jeans regime. A single ALMA S_{disk} value can significantly constrain β, however, more S_{disk} values at higher frequency bands would increase the precision and confidence of the result. This is especially true in galaxies like NGC 6861 that have minimal observations in the mid to far-IR. Higher resolution imaging in the 10^{13} to 10^{14} range would also reduce the risk of including diffuse dust populations separate from the CND in our CND analyses. This may fix the high β values seen in NGC 4261 and NGC 6861.

In conclusion, we find that the availability of high resolution ALMA data can help us constrain dust properties for CNDs in ETGs when using a MBB function. Comparisons to full-SED fitting programs like `CIGALE` show some discrepancies, although `CIGALE` has limitations such as the inability to fit global radio data alongside high resolution ALMA images of only the CND. Importantly, `CIGALE` shows that our assumptions of power-law-like emission from non-dust sources is supported. Additionally, when using ALMA data to determine mass or temperature gradients within the SED, we find that the more detailed analysis yields similar results to the standard isothermal fitting. We find that isothermal MBB fitting methods, when coupled with ALMA data, will be suitable for efficiently constraining dust properties larger samples in future projects.

Appendix A

Corner Plots

Corner plots are plot used to illustrate the output of `emcee` Bayesian fitting (see Section 2.2.1). Each corner plot shows a histogram for each fitted parameter. The histograms show the final position of each walker. The plots interior to the histograms are a sort of multi-dimensional histogram, where we can see the final position of walkers for two parameters instead of one. This helps us visualize any patterns or degeneracies between parameters. For example, it is mentioned in section 1.3 that there is a known degeneracy between β and T_d. Linear trends in our corner plots between β and T_d are evidence of this degeneracy. Figures A.1$-$A.5 show corner plots for the galaxies in our sample.
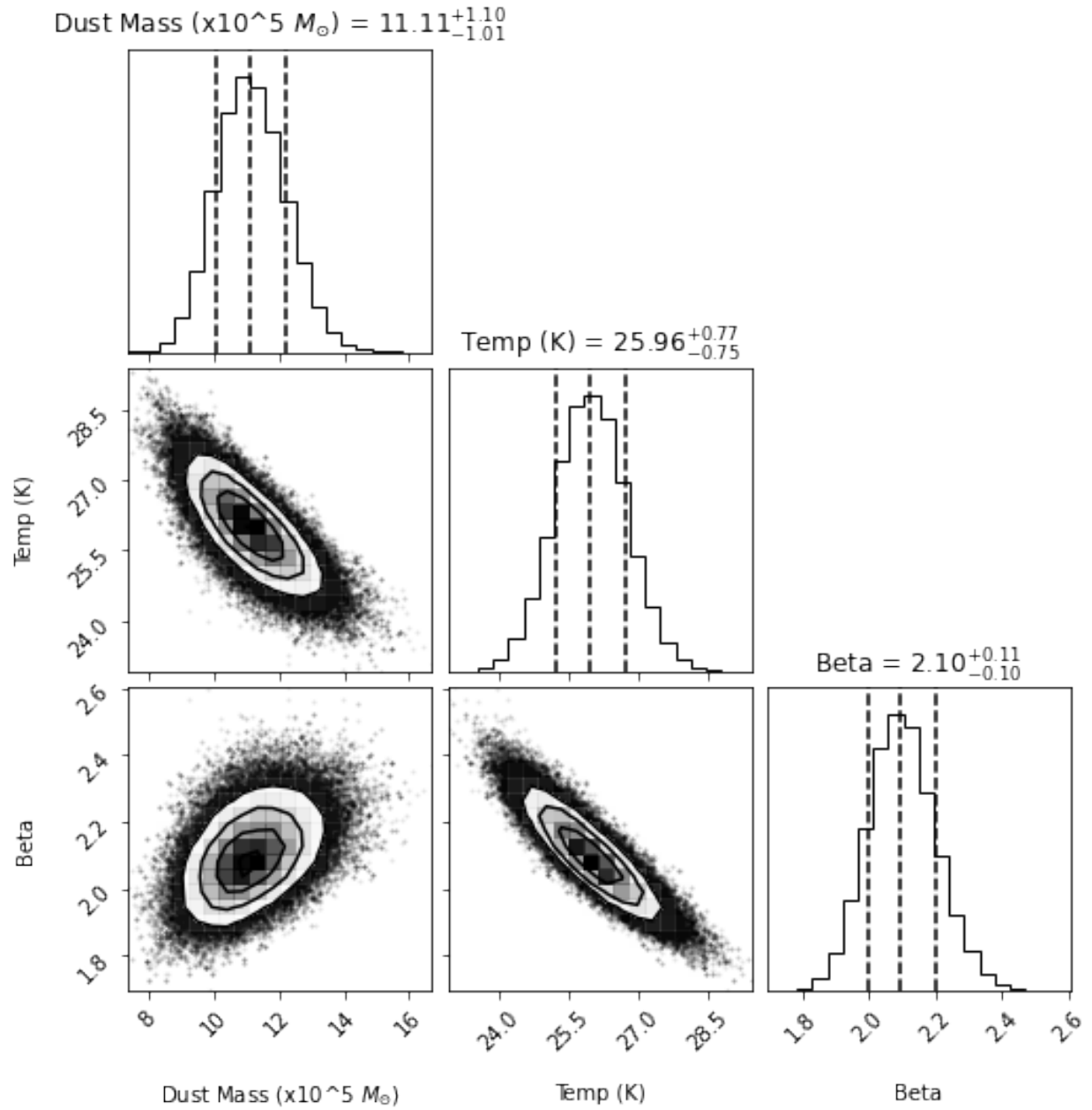
Figure A.1 The corner plot for NGC 1380.
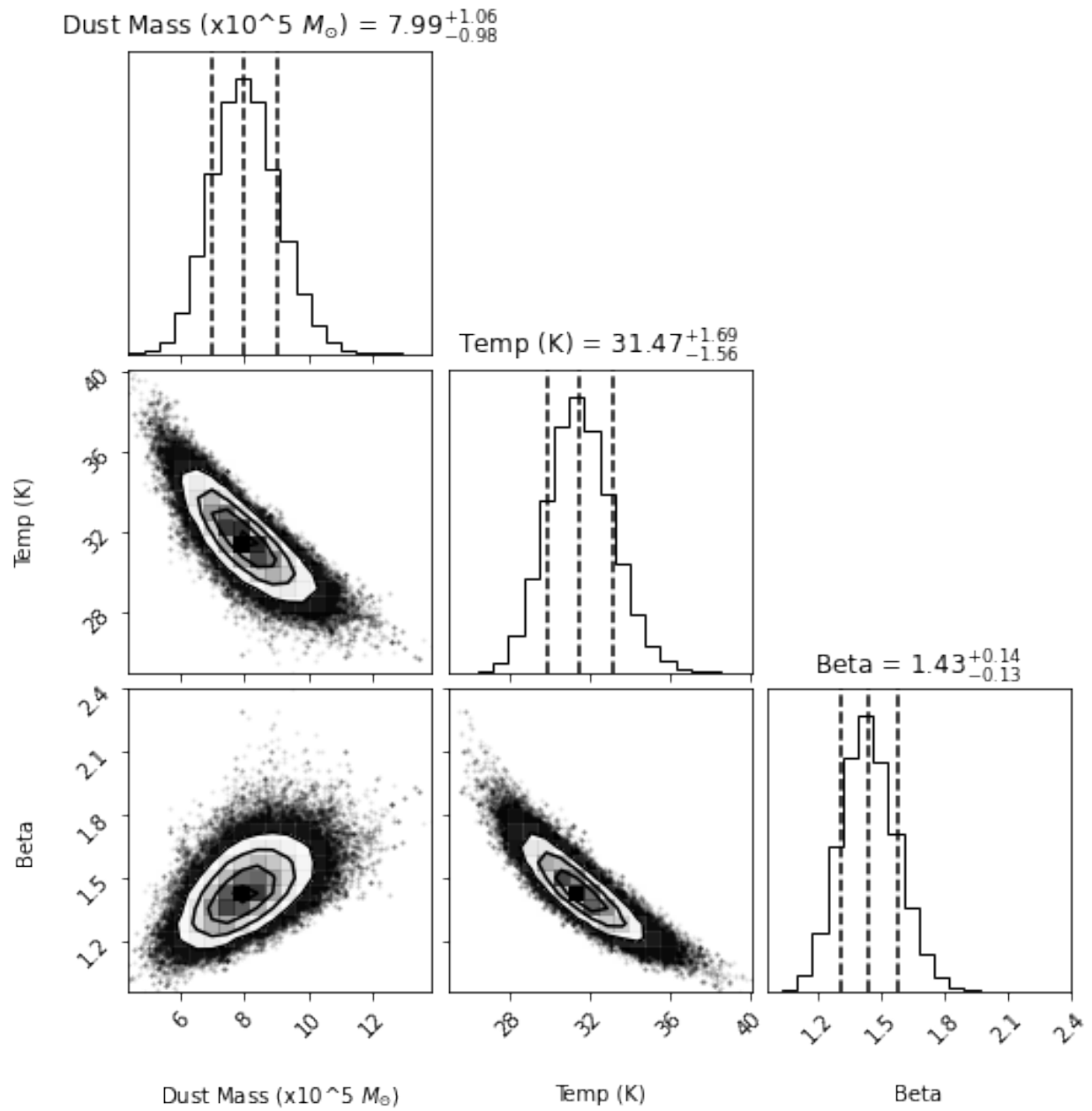
Figure A.2 The corner plot for NGC 3557.
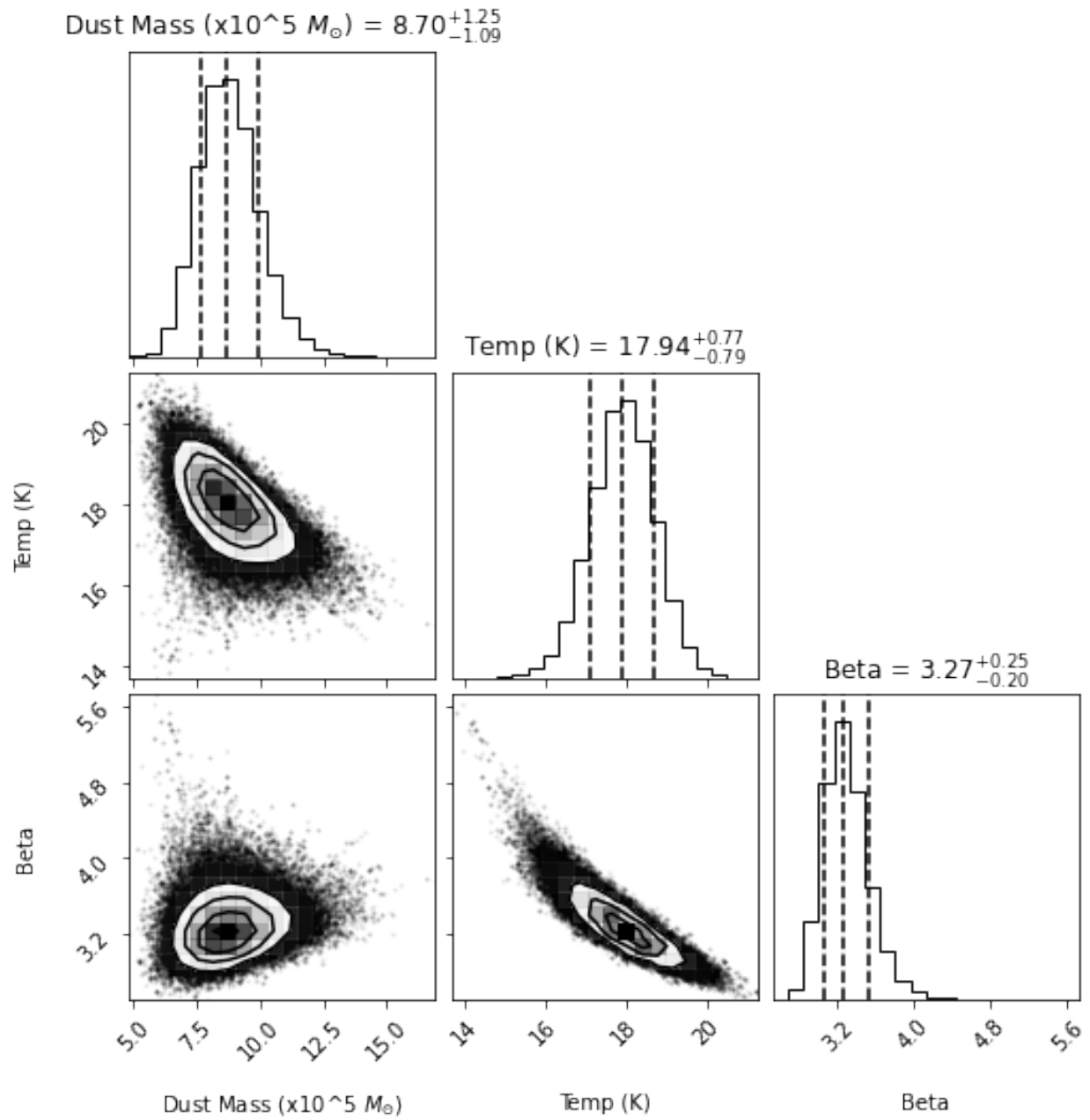
Figure A.3 The corner plot for NGC 4261.
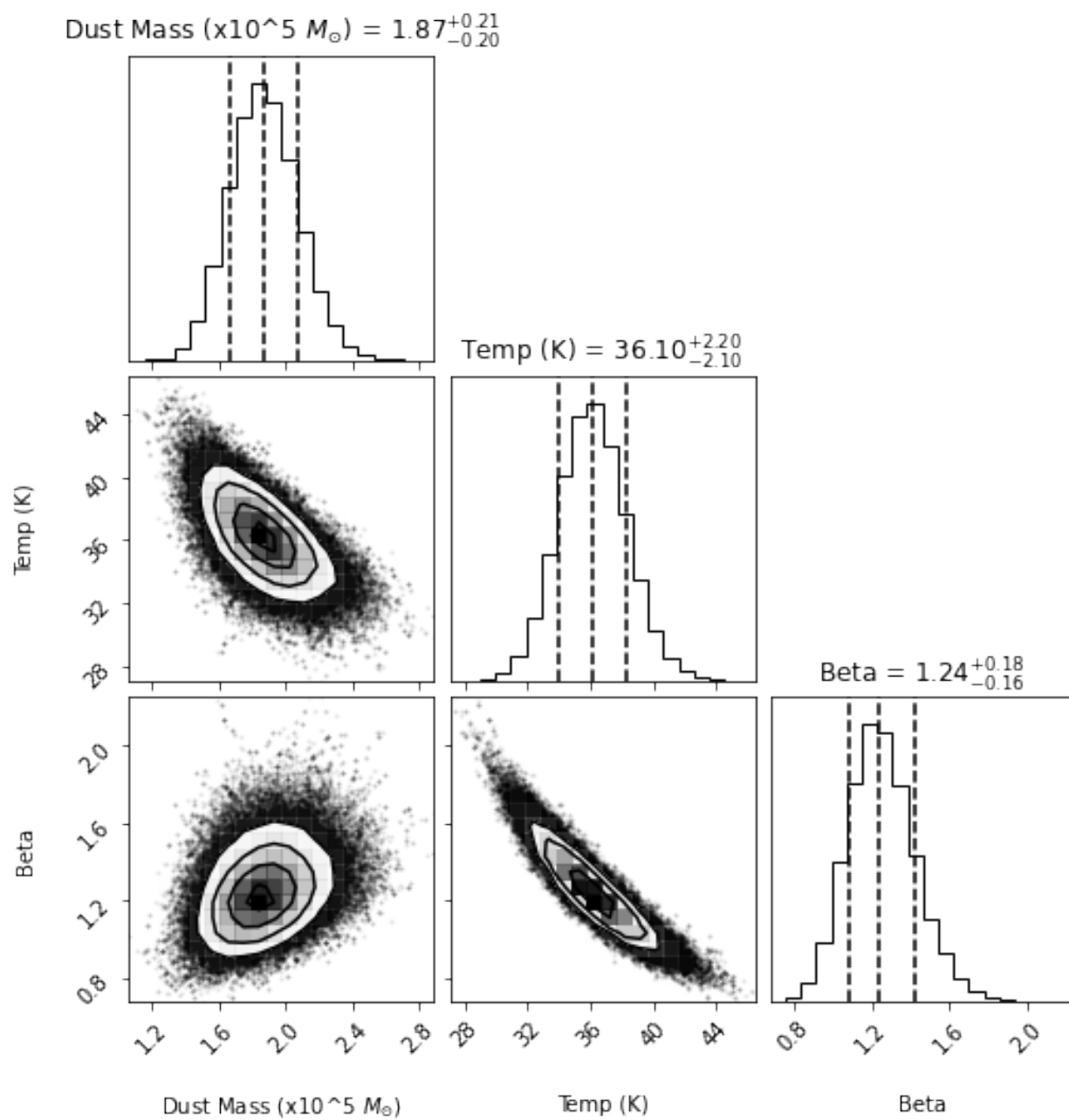
Figure A.4 The corner plot for NGC 4374.
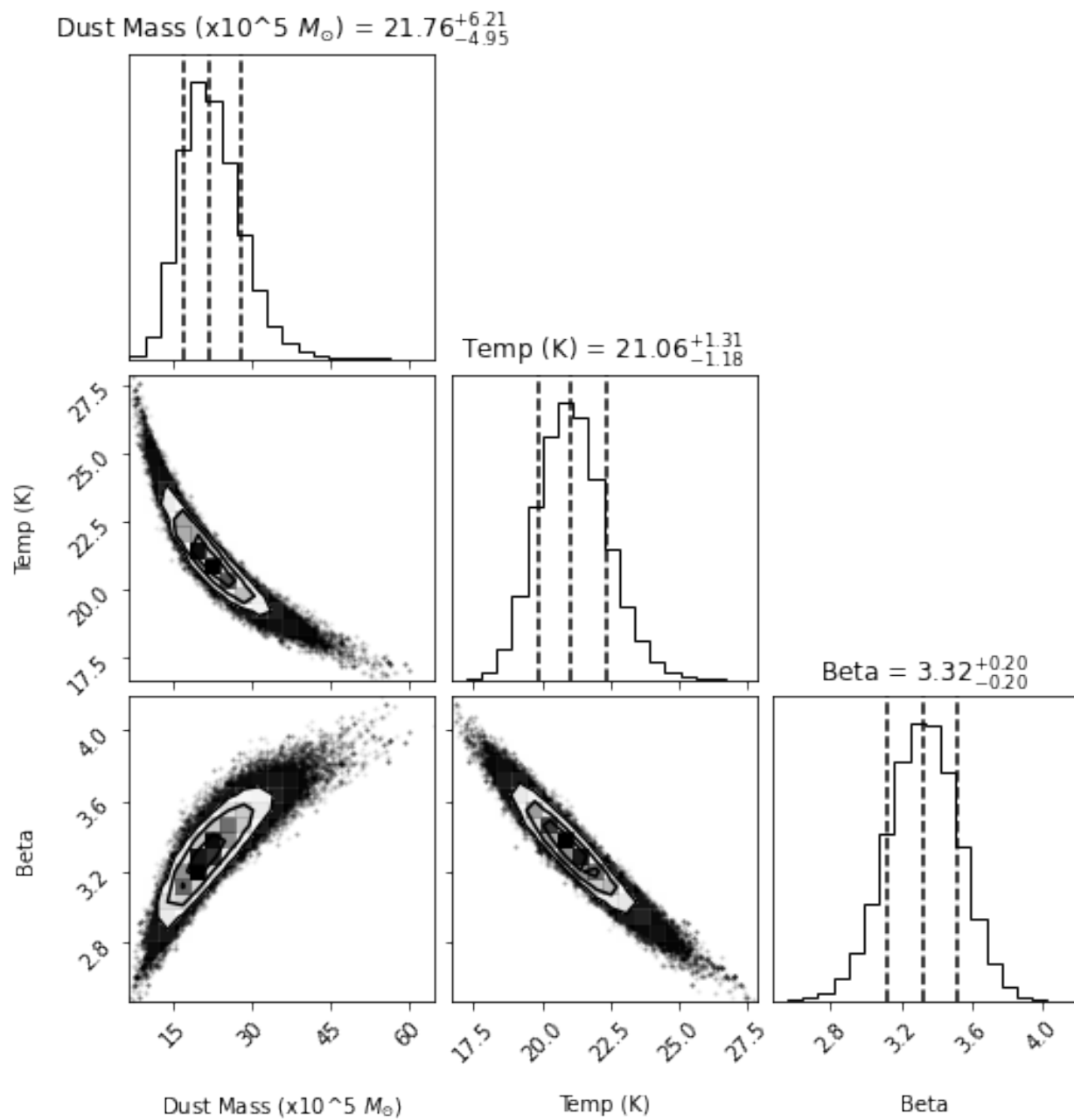
Figure A.5 The corner plot for NGC 6861.

Bibliography

[1] E. P. Hubble, "Extragalactic nebulae.," ApJ **64,** 321–369 (1926).

[2] Zooniverse, "Types of Galaxies," https://blog.galaxyzoo.org/2010/05/12/types-of-galaxies/ (Accessed February 28, 2023).

[3] S. di Serego Alighieri *et al.*, "The HI content of early-type galaxies from the ALFALFA survey. I. Catalogued HI sources in the Virgo cluster," A&A **474,** 851–855 (2007).

[4] P. Serra *et al.*, "The ATLAS^{3D} project - XIII. Mass and morphology of H I in early-type galaxies as a function of environment," MNRAS **422,** 1835–1862 (2012).

[5] L. M. Young *et al.*, "The ATLAS^{3D} project - IV. The molecular gas content of early-type galaxies," MNRAS **414,** 940–967 (2011).

[6] M. W. L. Smith *et al.*, "The Herschel Reference Survey: Dust in Early-type Galaxies and across the Hubble Sequence," ApJ **748,** 123 (2012).

[7] S. di Serego Alighieri *et al.*, "The Herschel Virgo Cluster Survey. XIII. Dust in early-type galaxies," A&A **552,** A8 (2013).

[8] T. Kokusho, H. Kaneda, M. Bureau, T. Suzuki, K. Murata, A. Kondo, M. Yamagishi, T. Tsuchikawa, and T. Furuta, "Dust properties in the cold and hot gas phases of the ATLAS^{3D} early-type galaxies as revealed by AKARI," A&A **622,** A87 (2019).

[9] H. D. Tran, Z. Tsvetanov, H. C. Ford, J. Davies, W. Jaffe, F. C. van den Bosch, and A. Rest, "Dusty Nuclear Disks and Filaments in Early-Type Galaxies," AJ **121,** 2928–2942 (2001).

[10] ESA/Hubble, "The third way of galaxies," https://esahubble.org/images/potw1502a/ (Accessed March 1, 2023).

[11] T. A. Davis *et al.*, "The ATLAS^{3D} project - X. On the origin of the molecular and ionized gas in early-type galaxies," MNRAS **417,** 882–899 (2011).

[12] B. T. Draine and E. E. Salpeter, "On the physics of dust grains in hot gas.," ApJ **231,** 77–94 (1979).

[13] M. S. Clemens *et al.*, "The Herschel Virgo Cluster Survey. III. A constraint on dust grain lifetime in early-type galaxies," A&A **518,** L50 (2010).

[14] B. D. Boizelle, A. J. Barth, J. Darling, A. J. Baker, D. A. Buote, L. C. Ho, and J. L. Walsh, "ALMA Observations of Circumnuclear Disks in Early-type Galaxies: ^{12}CO(2-1) and Continuum Properties," ApJ **845,** 170 (2017).

[15] T. A. Davis *et al.*, "The ATLAS^{3D} Project - XIV. The extent and kinematics of the molecular gas in early-type galaxies," MNRAS **429,** 534–555 (2013).

[16] T. A. Davis and M. Bureau, "On the depletion and accretion time-scales of cold gas in local early-type galaxies," MNRAS **457,** 272–280 (2016).

[17] A. Athey, J. Bregman, J. Bregman, P. Temi, and M. Sauvage, "Mid-Infrared Observation of Mass Loss in Elliptical Galaxies," ApJ **571,** 272–281 (2002).

[18] B. T. Draine, "Interstellar Dust Grains," ARAA **41,** 241–289 (2003).

[19] J. L. Tonry, A. Dressler, J. P. Blakeslee, E. A. Ajhar, A. B. Fletcher, G. A. Luppino, M. R. Metzger, and C. B. Moore, "The SBF Survey of Galaxy Distances. IV. SBF Magnitudes, Colors, and Distances," ApJ **546,** 681–693 (2001).

[20] V. Mennella, J. R. Brucato, L. Colangeli, P. Palumbo, A. Rotundi, and E. Bussoletti, "Temperature Dependence of the Absorption Coefficient of Cosmic Analog Grains in the Wavelength Range 20 Microns to 2 Millimeters," ApJ **496,** 1058–1066 (1998).

[21] N. Boudet, H. Mutschke, C. Nayral, C. Jäger, J. P. Bernard, T. Henning, and C. Meny, "Temperature Dependence of the Submillimeter Absorption Coefficient of Amorphous Silicate Grains," ApJ **633,** 272–281 (2005).

[22] R. Shetty, J. Kauffmann, S. Schnee, and A. A. Goodman, "The Effect of Noise on the Dust Temperature-Spectral Index Correlation," ApJ **696,** 676–680 (2009).

[23] L. K. Hunt *et al.*, "Cool dust heating and temperature mixing in nearby star-forming galaxies," A&A **576,** A33 (2015).

[24] M. Juvela and N. Ysard, "The effect of temperature mixing on the observable (T, β)-relation of interstellar dust clouds," A&A **539,** A71 (2012).

[25] F. Galliano, M. Galametz, and A. P. Jones, "The Interstellar Dust Properties of Nearby Galaxies," ARAA **56,** 673–713 (2018).

[26] A. J. Barth, B. D. Boizelle, J. Darling, A. J. Baker, D. A. Buote, L. C. Ho, and J. L. Walsh, "Measurement of the Black Hole Mass in NGC 1332 from ALMA Observations at 0.044 arcsecond Resolution," ApJL **822,** L28 (2016).

[27] B. D. Boizelle, A. J. Barth, J. L. Walsh, D. A. Buote, A. J. Baker, J. Darling, and L. C. Ho, "A Precision Measurement of the Mass of the Black Hole in NGC 3258 from High-resolution ALMA Observations of Its Circumnuclear Disk," ApJ **881,** 10 (2019).

[28] E. V. North, T. A. Davis, M. Bureau, M. Cappellari, S. Iguchi, L. Liu, K. Onishi, M. Sarzi, M. D. Smith, and T. G. Williams, "WISDOM project - V. Resolving molecular gas in Keplerian rotation around the supermassive black hole in NGC 0383," MNRAS **490,** 319–330 (2019).

[29] B. D. Boizelle, J. L. Walsh, A. J. Barth, D. A. Buote, A. J. Baker, J. Darling, L. C. Ho, J. Cohn, and K. M. Kabasares, "Black Hole Mass Measurements of Radio Galaxies NGC 315 and NGC 4261 Using ALMA CO Observations," ApJ **908,** 19 (2021).

[30] L. Liu, M. Bureau, L. Blitz, T. A. Davis, K. Onishi, M. Smith, E. North, and S. Iguchi, "WISDOM Project - IX. Giant molecular clouds in the lenticular galaxy NGC 4429: effects of shear and tidal forces on clouds," MNRAS **505,** 4048–4085 (2021).

[31] A. Hirota, F. Egusa, J. Baba, N. Kuno, K. Muraoka, T. Tosaki, R. Miura, H. Nakanishi, and R. Kawabe, "ALMA ^{12}CO (J = 1-0) imaging of the nearby galaxy M 83: Variations in the efficiency of star formation in giant molecular clouds," PASJ **70,** 73 (2018).

[32] I. Ruffa, I. Prandoni, R. A. Laing, R. Paladino, P. Parma, H. de Ruiter, A. Mignano, T. A. Davis, M. Bureau, and J. Warren, "The AGN fuelling/feedback cycle in nearby radio galaxies I. ALMA observations and early results," MNRAS **484,** 4239–4259 (2019).

[33] C. B. Markwardt, "Non-linear Least-squares Fitting in IDL with MPFIT," In *Astronomical Data Analysis Software and Systems XVIII*, D. A. Bohlender, D. Durand, and P. Dowler, eds., Astronomical Society of the Pacific Conference Series **411,** 251 (2009).

[34] D. Foreman-Mackey, D. W. Hogg, D. Lang, and J. Goodman, "emcee: The MCMC Hammer," PASP **125,** 306 (2013).

[35] S. Noll, D. Burgarella, E. Giovannoli, V. Buat, D. Marcillac, and J. C. Muñoz-Mateos, "Analysis of galaxy spectral energy distributions from far-UV to far-IR with CIGALE: studying a SINGS test sample," A&A **507,** 1793–1813 (2009).

[36] M. Boquien, D. Burgarella, Y. Roehlly, V. Buat, L. Ciesla, D. Corre, A. K. Inoue, and H. Salas, "CIGALE: a python Code Investigating GALaxy Emission," A&A **622,** A103 (2019).

[37] G. Yang, M. Boquien, V. Buat, D. Burgarella, L. Ciesla, F. Duras, M. Stalevski, W. N. Brandt, and C. Papovich, "X-CIGALE: Fitting AGN/galaxy SEDs from X-ray to infrared," MNRAS **491,** 740–757 (2020).

[38] G. Bruzual and S. Charlot, "Stellar population synthesis at the resolution of 2003," MNRAS **344,** 1000–1028 (2003).

[39] G. Chabrier, "Galactic Stellar and Substellar Initial Mass Function," PASP **115,** 763–795 (2003).

[40] B. T. Draine and A. Li, "Infrared Emission from Interstellar Dust. IV. The Silicate-Graphite-PAH Model in the Post-Spitzer Era," ApJ **657,** 810–837 (2007).

[41] B. T. Draine *et al.*, "Andromeda's Dust," ApJ **780,** 172 (2014).

[42] M. Stalevski, J. Fritz, M. Baes, T. Nakos, and L. Č. Popović, "3D radiative transfer modelling of the dusty tori around active galactic nuclei as a clumpy two-phase medium," MNRAS **420,** 2756–2772 (2012).

[43] M. Stalevski, C. Ricci, Y. Ueda, P. Lira, J. Fritz, and M. Baes, "The dust covering factor in active galactic nuclei," MNRAS **458,** 2288–2302 (2016).

[44] C. L. Carilli and F. Walter, "Cool Gas in High-Redshift Galaxies," ARAA **51,** 105–161 (2013).

[45] K. M. Sandstrom *et al.*, "The CO-to-H_2 Conversion Factor and Dust-to-gas Ratio on Kiloparsec Scales in Nearby Galaxies," ApJ **777,** 5 (2013).

[46] F. F. S. van der Tak, J. H. Black, F. L. Schöier, D. J. Jansen, and E. F. van Dishoeck, "A computer program for fast non-LTE analysis of interstellar line spectra. With diagnostic plots to interpret observed line intensity ratios," A&A **468,** 627–635 (2007).

Index